Volume 12 | Number 15 | 7 August 2025

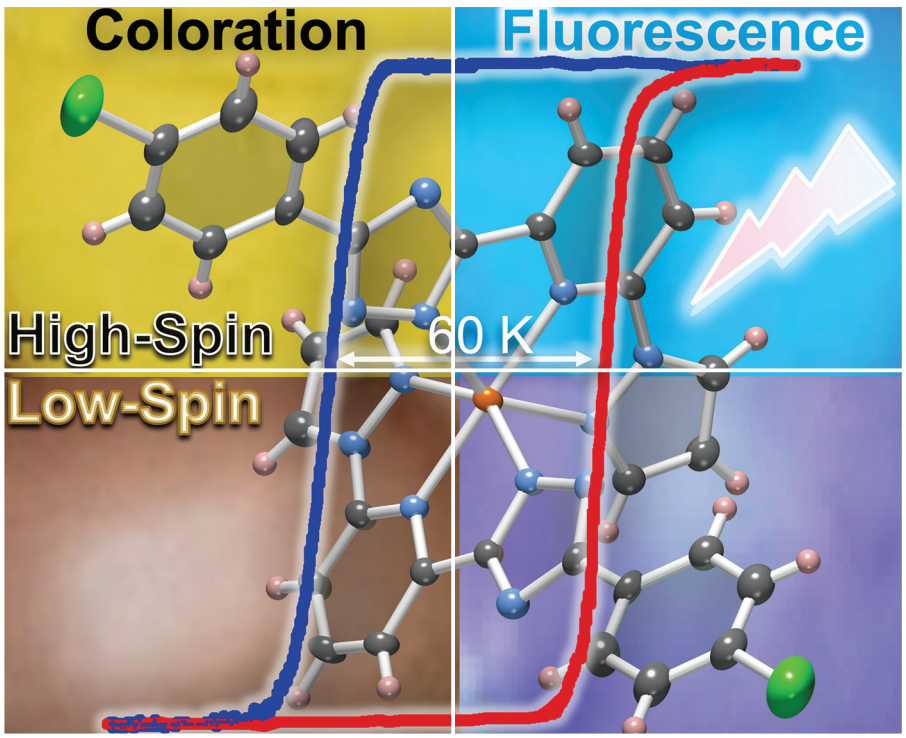

INORGANIC CHEMISTRY

FRONTIERS

CCS 中国化学会 CHINESE CHEMICAL SOCIETY
PEKING UNIVERSITY 1898
ROYAL SOCIETY OF CHEMISTRY
rsc.li/frontiers-inorganic

INORGANIC CHEMISTRY FRONTIERS

RESEARCH ARTICLE

View Article Online
View Journal | View Issue

Cite this: *Inorg. Chem. Front.*, 2025, **12**, 4583

60 K wide hysteresis embracing room temperature in a fluorescent Fe^{II} spin transition complex†

Maksym Seredyuk, *[a] Kateryna Znovjyak, [a] Francisco Javier Valverde-Muñoz, [b,g] M. Carmen Muñoz, [c] Teresa Delgado, [d,e] Ivan da Silva [f] and José Antonio Real *[g]

This work presents the synthesis and characterization of a new neutral mononuclear Fe(II) spin transition (ST) complex, $[Fe^{II}(L)_2]^0$ (**4Cl**), where L is an asymmetrically substituted tridentate ligand 2-(3-(4-chlorophenyl)-1*H*-1,2,4-triazol-5-yl)-6-(1*H*-pyrazol-1-yl)pyridine. **4Cl** exhibits a remarkably wide stable ST hysteresis loop *ca.* 60 K wide embracing room temperature ($T^{\uparrow}_{1/2}$ = 308 K and $T^{\downarrow}_{1/2}$ = 248 K). Detailed structural, calorimetric and spectroscopic investigations, including X-ray diffraction with Rietveld analysis, Raman spectroscopy, and photoluminescence, reveal the crucial role of subtle structural changes within the crystal lattice in driving the cooperative spin transition. The DFT energy framework analysis highlights the interplay of balanced stabilizing and destabilizing intermolecular interactions that contribute to the observed hysteresis. Furthermore, the fluorescent properties of **4Cl** exhibit distinct changes in emission intensity and wavelength upon spin state switching with emission color change from sky blue in the high spin state to violet in the low spin state. The compound is the first example of the spin transition compound with bistable fluorescence response at room temperature.

Received 28th March 2025,
Accepted 3rd June 2025

DOI: 10.1039/d5qi00856e

rsc.li/frontiers-inorganic

Introduction

Six-coordinated Fe^{II} spin transition (ST) complexes, reversibly switch between the paramagnetic high-spin $^5T_{2g}$ [HS, $t_{2g}^4e_g^2$ (S = 2)] and the diamagnetic low-spin $^1A_{1g}$ [LS, $t_{2g}^6e_g^0$ (S = 0)] states by the action of thermal and/or pressure gradients, light irradiation, electric fields and analytes. The internal two-electron transfer involved between the $t_{2g} \leftrightarrow e_g$ orbitals is strongly coupled with a change of the Fe^{II} ionic radius, being *ca.* 0.2 Å smaller in the LS state. This structural mismatch between both spin states is in the background of the cooperatively leading to the occurrence of hysteretic behavior (memory effect) in the magnetic, calorimetric, optical, electrical and elastic properties in appropriate ST complexes.[1] These features have made Fe^{II} ST complexes an excellent platform to afford new advanced materials particularly attractive for potential applications such as displays, sensors, actuators, information storage, thermal management and spintronics.[2] For practical reasons, the bistability window should be centered around room temperature (RT) and enclose or even exceed the operating temperature of the device. Both conditions severely limit the number of useful ST complexes available. The main reason is that the design of such complexes with predetermined transition temperature and hysteresis width, and especially with an additional function, remains an elusive task due to the inherent synthetic difficulties associated with the control of supramolecular interactions in the solid state.[3] In spite of this, hysteresis loops wider than 40 K have been described for a few mononuclear[4] and polymeric[5] Fe^{II} ST complexes. It is worth noting that most of these referred mononuclear complexes are made up of planar tridentate ligands of the bispyrazole-pyridine type which apparently facilitates molecular packing suitable for the cooperative transmission of the structural changes during the ST event.

Combination of hysteretic transition with a second property such as electric conductivity,[6] magnetic,[7] or nonlinear optic response[8] is also actively studied by the community. Particularly, fluorescence combined with the ST provides a type of functional materials which enable sensitive detection

[a]*Department of Chemistry, Taras Shevchenko National University of Kyiv, Kyiv 01601, Ukraine. E-mail: maksym.seredyuk@knu.ua*
[b]*Departament Matériaux et Lumière Institut de Physique de Rennes Université de Rennes 1, UMR UR1-CNRS 6251, 35000 Rennes, France*
[c]*Departamento de Física Aplicada, Universitat Politècnica de València, Camino de Vera s/n, E-46022 Valencia, Spain*
[d]*PSL University, Chimie ParisTech – CNRS, Institut de Recherche de Chimie Paris, 11 Rue Pierre et Marie Curie, Paris 75005, France*
[e]*Pharmacy Department, CEU Cardenal Herrera University, CEU Universities C/ Ramón y Cajal s/n, Alfara del Patriarca, 46115 Valencia, Spain*
[f]*ISIS Neutron Facility, STFC Rutherford Appleton Laboratory, Chilton, Oxfordshire, OX11 0QX, UK*
[g]*Instituto de Ciencia Molecular, Departamento de Química Inorgánica, Universidad de Valencia, 46980 Paterna, Valencia, Spain. E-mail: jose.a.real@uv.es*

†Electronic supplementary information (ESI) available. CCDC 2416064, 2416066 and 2424238. For ESI and crystallographic data in CIF or other electronic format see DOI: https://doi.org/10.1039/d5qi00856e

of spin-state changes through the emission wave-length.[9] A possible application in magneto-optical switching or thermos-sensors can benefit from a possibility to probe the local change by monitoring the emitted wavelength and/or emission intensity upon the ST event down to the molecular scale.

Achieving a strong coupling between luminescence and the spin states in a single system presents a significant challenge, as it is difficult to keep desired ST properties, usually completeness and bistability (hysteresis), and yet achieve interplay with the luminescence. To this end, the two main strategies are used to achieve the coupling of the properties, consisting in combining mechanically, by inclusion, or by grafting fluorescent species and ST materials or, alternatively, synthesizing ST complexes with fluorescent ligands.[10] Although several known fluorophores (dansyl, pyrene, anthracene, chlorophyll *etc.*) were successfully tested in such hybrid ST systems, including nanoparticles,[11] thin films,[12] metal–organic frameworks,[13] the interplay between the two events is usually weak, resulting in minor variations in fluorescent intensity.

Already the very first studies on fluorescent ST complexes revealed applicability of ligands as fluorophores[14] and substantiated later by theoretical studies.[15] Despite the native ligand fluorescence can be quenched in both HS and LS states or no synergism between the fluorescence and ST properties can be observed in this case,[16] the ligand usually bears an essential flexibility for chemical modification as can be varied to balance the structural constraints and facilitate the occurrence of the both phenomena with required characteristics. Achieving a fixed ratio between the fluorophore and chromophore [FeN_6], and also a fixed but adjustable distance between the two by the ST transition, afforded a few systems with evident coupling of the phenomena in molecular,[2c,4i,14,17] and polymeric complexes.[5c,18] In contrast to the coupling described above, the fluorescent variation is not only changing the intensity, but also the wavelength of the fluorescent band with a change of the coloration of emitted light.[2c,5c]

While the rational design of ligands that integrate intrinsic fluorescence with cooperative ST behavior holds promise, the number of known complexes exhibiting bistable fluorescence response remains limited,[5c,13c] with none operating at RT. In this context, we recently reported on neutral mononuclear Fe^{II} ST complexes, $[Fe^{II}(L)_2]^0 \cdot n$MeOH (n = 0–2), based on asymmetrically substituted large planar ionogenic ligands L, containing the R-(1*H*-1,2,4-triazol-5-yl)-6-(1*H*-pyrazol-1-yl)pyridine coordination core with R = 3-methoxyphenyl[19] or 2-fluorophenyl[20] (see Scheme 1) with distinctive cooperativity. In general, this type of complexes favors a similar molecular packing in which it is possible to systematically explore specific R substituents for the capability to induce appealing cooperative ST phenomenologies. Our studies have found that with 4-chlorophenyl substituent (Scheme 1) the Fe^{II} complex is hysteretic with a 60 K wide loop and is additionally fluorescent, emitting sky blue or violet light depending on the spin state, visible to the naked eye. To the best of our knowledge, this is the first instance of an ST compound exhibiting bistable fluorescence at room temperature.

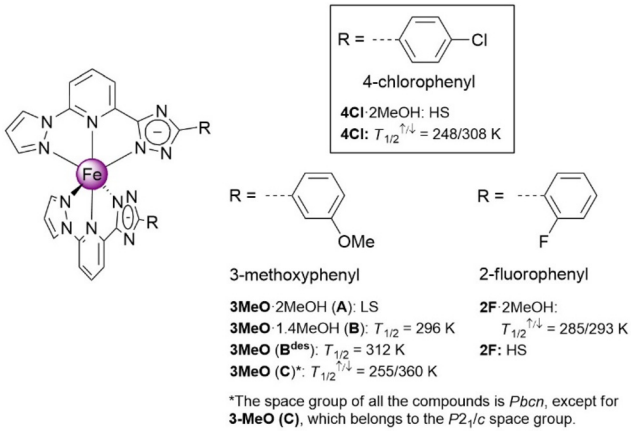

Scheme 1 Structural formula of the $[Fe^{II}(L)_2]^0$ complexes with the pyrazol-pyridine-triazolate core and the peripheral R = 3-methoxy-, 2-fluoro- and 4-chloro-phenyl substituents. Additionally, the respective spin states or transition temperatures are indicated (see the text for details).

Results

Synthesis

The synthesis of the complex proceeds from an Fe^{II} salt and the ligand L = 2-(3-(4-chlorophenyl)-1*H*-1,2,4-triazol-5-yl)-6-(1*H*-pyrazol-1-yl)pyridine, that affords a highly crystalline sample of the solvate $[Fe^{II}L_2]\cdot 2$MeOH, (**4Cl**·2MeOH), which was characterized *via* single crystal diffraction analysis (*vide infra*). Complete desolvation, taking place by gently heating this sample at 400 K, irreversibly affords desolvated **4Cl**, whose thermal analysis (see Fig. S1†) demonstrates remarkable thermal stability (up to 600 K). **4Cl** has been characterized through elemental analysis and Rietveld refinement from the experimental powder X-ray diffraction (PXRD) data (*vide infra*).

Magnetic, photomagnetic and optical reflectance measurements

The magnetic properties of the **4Cl**·2MeOH and the desolvated complex **4Cl** are depicted in Fig. 1 as the product $\chi_M T$ *vs.* T, where χ_M is the molar magnetic susceptibility and T is the temperature. The temperature scan rate was 2 and 0.3 K min^{-1} for **4Cl**·2MeOH and **4Cl**, respectively. For **4Cl**·2MeOH the $\chi_M T$ value is *ca.* 3.28 cm^3 K mol^{-1} and remains practically constant in the temperature interval 300–50 K indicating that the Fe^{II} centres are in the HS state. The slight decrease below 50 K is associated with the zero-field splitting. Similarly, the $\chi_M T$ value of **4Cl**, *ca.* 3.38 cm^3 K mol^{-1}, remains constant in the interval 350–260 K. When cooling below 260 K, $\chi_M T$ drastically drops to attain a value *ca.* 0.1 cm^3 K mol^{-1} at around 228 K. Both extreme values are consistent with the HS and LS state of the Fe^{II} ion, respectively. In the heating mode, the $\chi_M T$ *versus* T profile does not match the cooling mode defining a hysteresis *ca.* 60 K wide. The characteristic temperatures, $T_c^{\downarrow}$ and $T_c^{\uparrow}$ of the strong cooperative ST calculated as the maximum of the $\delta(\chi_M T)/\delta T$ *vs.* T function are 248 K and 308 K (T_c^{av} = 278 K),

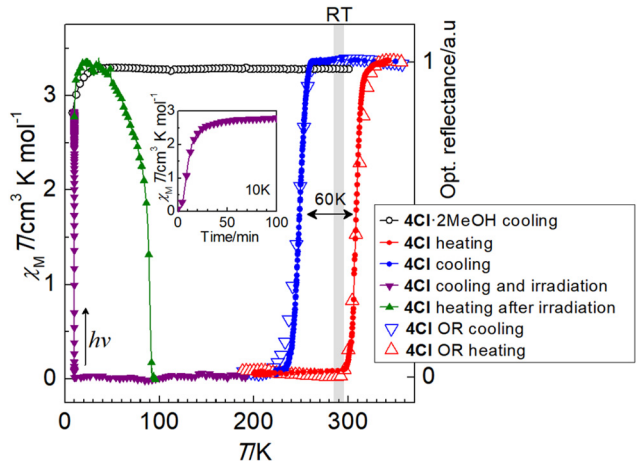

Fig. 1 Magnetic, photomagnetic and optical reflectance properties of compounds **4Cl**·MeOH and **4Cl**; the inserted graph shows the $\chi_M T$ *vs.* time saturation curve during the LIESST irradiation.

respectively. The stability of this remarkably wide hysteresis loop was confirmed by performing 8 cycles at 4 K min^{-1} (see Fig. S2†).

As **4Cl** is highly thermochromic and exhibits a color change from brown in the LS state to yellow in the HS state (see diffuse reflectance spectra in Fig. S3†), the coloration change can also be used to monitor the thermal evolution of the spin states ratio during the ST.[21] The normalized optical reflectance (OR) followed as the function of temperature is overlaid with magnetic data in Fig. 1. The determined characteristic temperatures, $T_c^{\downarrow}$(OR) = 247 K and $T_c^{\uparrow}$(OR) = 309 K perfectly coincide with the values obtained in magnetic measurements. Optical images of **4Cl**, taken at room temperature in both spin states clearly demonstrate the thermochromic effect caused by the ST (*vide infra*).

Photogeneration of the metastable HS* state from the LS state, the so-called light induced excited spin state trapping (LIESST) experiment,[22] was performed at 10 K irradiating a microcrystalline sample of **4Cl** with green light (λ = 532 nm). The sample undergoes quantitative (100%) LIESST effect with $\chi_M T$ saturating to a value of *ca.* 2.81 cm^3 K mol^{-1}. Subsequently, the light was switched off and the temperature increased at a rate of 0.3 K min^{-1} inducing a gradual increase in $\chi_M T$ reaching a maximum value of 3.36 cm^3 K mol^{-1} in the interval of 10–39 K. This increase in $\chi_M T$ reflects the thermal population of different microstates originating from the zero-field splitting of the HS* state. Above 39 K, $\chi_M T$ decreases rapidly upon heating until it joins the ST thermal curve at *ca.* 92 K, indicating that the metastable HS* state has relaxed back to the stable LS state. The corresponding T_{LIESST} temperatures, evaluated as $\delta(\chi_M T)/\delta T$,[23] is 90 K.

It was demonstrated that a linear correlation between the ST equilibrium temperature $T_{1/2}$ and T_{LIESST} generally holds for different types of Fe^{II} complexes. In particular, for complexes with tridentate ligands, the two physical quantities can be related by the empirical formula: $T_{LIESST} = T_0 - 0.3T_{1/2}$, where $T_0 \approx 150$ K.[24] The calculated value $T_0 = T_{LIESST} + 0.3T_{1/2}$ for **4Cl** is close to this, being equal to *ca.* 173 K.

Raman spectra

To have a deeper insight into the nature of the ST in **4Cl**, variable temperature Raman spectroscopy was performed. Fig. 2 displays the LS (225 K) and HS (325 K) normalized spectra in the interval of 400–1680 cm^{-1} (λ = 532 nm, 0.01726 mW). This vibrational window is dominated by synchronized deformation modes of the rings of the ligands. There are two significant vibrations which display drastic changes upon spin conversion. The peaks at 1012 and 1381 cm^{-1} are characteristic of the HS state and attain a maximum intensity at 325 K, however, they vanish at expense of the appearance of a peak at, respectively, 1032 and 1366 cm^{-1} associated with the LS state where attain a maximum intensity (see Fig. 2). These Raman spectra are consistent with those reported for other related Fe^{II} ST complexes with similar tridentated bispyrazolyl pyridine ligands.[4k,25]

An attempt to track the thermal evolution of the characteristic HS/LS Raman vibrational has failed due to the high sensitivity of the compound to the laser irradiation which tends to distort the hysteresis loop (Fig. S4a–c†). For an intensity of 1% (0.0173 mW) the main features of the ST, *i.e.* average characteristic temperature, $T_c^{av} \approx 280$ K and strong cooperativity, are reasonably well reproduced. However, the characteristic temperatures observed for the heating/cooling branches are shifted *ca.* 20 K below/above with respect to the hysteresis loop observed from $\chi_M T$ *vs.* T plots, thereby defining these selected markers a hysteresis loop 20 K wide. When the power is increased till 10% (0.1957 mW), $T_c^{av} \approx 250$ K, is more narrowed and significantly shifted to low temperatures. Finally, for a power of 25% (0.4286 mW) the compound does not experience ST remaining HS. Incomplete HS–LS transformation was detected when using a 633 nm laser (10% 0.6249 mW) (see Fig. S5†).

It is worth noting that the intensities of the Raman spectra are strongly influenced by the fluorescence emission (*vide infra*). Indeed, a dramatic decrease intensity of the

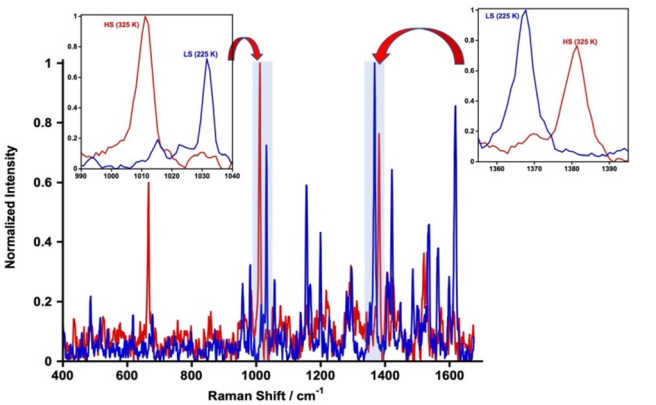

Fig. 2 Raman spectra of **4Cl** in the HS/LS state (325/225 K; red/blue). The inserted plots correspond to the magnification of the characteristic peaks at 1012, 1032 and 1366 cm^{-1} which markedly change with the spin state.

spectra baseline takes place when cooling from 275 to 265 K reflecting the change of optical properties upon HS to LS state switch. The reverse change in the baseline (*i.e.* luminescence) occurs when heating from 285 to 295 K (see Fig. S6†).

Calorimetric properties

The thermal dependence of the heat capacity at constant pressure, ΔC_p, for **4Cl** was monitored through differential scanning calorimetric (DSC) measurements recorded at 10 K min^{-1} (see Fig. 3). The average enthalpy ΔH and entropy variations ΔS (=$\Delta H/T_c$) (with T_c being the temperature at the maximum/minimum of ΔC_p *vs.* T plot) associated with the *exo*- and *endo*-thermic peaks are, respectively, 17.4 kJ mol^{-1} and 62.0 J K^{-1} mol^{-1}. These ΔH and ΔS values are consistent with the occurrence of a cooperative complete ST, in particular, ΔS is significantly higher than expected from electronic considerations (spin degeneracy only: $^1A_1 \rightarrow {}^5T_2$ transition, $\Delta S^{electr} = R\,Ln(5)$ = 13.4 J K^{-1} mol^{-1}). The remaining entropy variation (62.0–13.4 = 48.6 J K^{-1} mol^{-1}) accounts for the crystal and molecular vibrational modes involved in the ST process.[26] The $T_c^{av} = (T_c^{\downarrow} + T_c^{\uparrow})/2$ = (262 + 303)/2 = 282.5 K obtained from DSC data agree reasonably well with that, 278 K, obtained from magnetic measurements. It is important to remark that, in this case, the maximum/minimum of the DSC *vs.* T plot reflects, respectively, to the onset of the sudden drop (cooling)/rise (heating) of the $\chi_M T$ curves (Fig. 1). Consequently, the separation between the peaks in DSC is 40 K while the hysteresis width calculated through the derivative of $\chi_M T$, 60 K, is markedly larger. However, it is important to remark that the combined plot $\chi_M T - \Delta C_p$ *vs.* T (Fig. S7†) clearly shows the consistency between both measurements.

Crystal structure

Structure of 4Cl·2MeOH. The single crystal structure of **4Cl**·2MeOH was measured at 293 K where the crystal adopts the orthorhombic *Pbcn* space group. Relevant crystallographic data are summarised in Table S1† and Table 1 gathers selected bond lengths and angles as well as the most relevant geometrical parameters concerning the [Fe^{II}N$_6$] octahedral site. Fig. 4 displays the molecular structure together with the atom numbering. The average bond length $\langle Fe–N\rangle^{av}$ = 2.171 Å, the sum of the deviation from 90° of the 12 *cis* N–Fe–N angles of the coordination core $\Phi = \sum_1^{12} |\varphi_i - 90| = 148°$ at 293 K and the trigonal distortion parameter, $\Theta = \sum_1^{24} |\theta_i - 60| = 486°$, θ_i being the angle generated by superposition of two opposite faces of the octahedron, are consistent with the HS state observed from magnetic data. The dihedral angle, α, between the average planes defined by the pyrazole-pyridine-triazole (pptr) rings of the two ligands is 87.8°, furthermore the 4-Clph moieties display an angle β = 23.6° with respect to the average pptr plane.

Table 1 Selected bond lengths and angles as well as geometrical parameters involving the [FeN$_6$] coordination core of **4Cl**·2MeOH and **4Cl**

Bond lengths/Å	**4Cl**·2MeOH	**4Cl** (HS)	**4Cl** (LS)
Fe1–N1	2.233(6)	2.342(5)	1.962(6)
Fe1–N2	2.144(5)	2.118(5)	1.928(6)
Fe1–N3	2.136(5)	2.147(5)	1.906(5)
$\langle Fe–N\rangle^v$	2.171	2.202	1.932
Bond angles/°			
N1–Fe1–N2	72.0(2)	76.9(2)	79.0(3)
N1–Fe1–N3	92.1(2)	82.1(2)	94.1(2)
N1–Fe1–N1′	93.9(3)	99.3(2)	83.8(2)
N1–Fe1–N2′	103.3(2)	104.9(2)	100.4(3)
N1–Fe1–N3′	147.3(2)	152.9(4)	158.7(4)
N2–Fe1–N3	75.3(2)	76.6(4)	80.6(5)
N2–Fe1–N2′	173.4(3)	177.3(3)	179.1(4)
N2–Fe1–N3′	109.1(2)	101.8(4)	100.0(5)
N3–Fe1–N3′	99.9(3)	108.91(19)	95.3(2)
Geometrical parameters			
Φ/°	148	150.4	101.3
Θ/°	486	390	292
α/°	87.8	100.1	85.8
β/°	23.6	23.1	10.9

Like the previously described homologous complexes,[19,20] the molecules display a conical shape with a smaller part ("head") defined by two pyrazole (pz) rings and two longer divergent "tails" ending at the 4-phenyl (ph) groups attached to the triazole ring of the tridentate ligands linked by the Fe^{II} ion. The head of every molecule fits the cavity generated between the tails of the next neighbor molecule defining columns running along *b*. In each column, two consecutive complexes define a rectangular void characterized by a Fe···Fe distance of 10.101 Å, which corresponds to the cell parameter *b* (Fig. 5a). The molecules of neighboring columns laying in the same *a*–*b* plane, stack along *a*-direction filling the rectangular void, from both sides, through the pyridine moieties, consequently two adjacent 1D columns are shifted *b*/2 relatively to each other (Fig. 5b).

In addition, two methanol molecules per complex partially fill the remaining voids running along *b* axis. The packing of two consecutive supramolecular layers is shown in Fig. 5c. This supramolecular arrangement facilitates the occurrence of

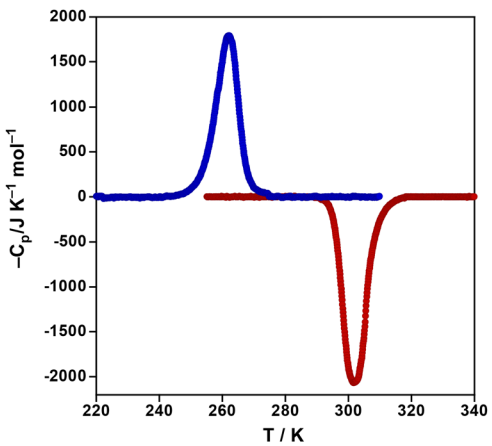

Fig. 3 Differential scanning calorimetric DSC plot as a function T in the cooling (blue)/heating (red) for 4Cl.

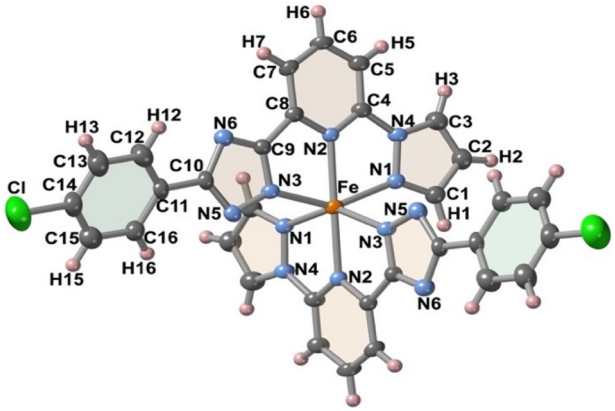

Fig. 4 Molecular structure of the coordination environment of **4Cl**·2MeOH showing the atom numbering of the asymmetric units (the MeOH molecules have been omitted).

short contacts (see Table S2†), smaller than the sum of the corresponding van der Waals radii (2.9 Å), between the pyrazole (head) and 4Cl-Ph (tail) rings belonging to consecutive molecules within the column, d(H2···C15) = 2.760 Å. In addition, the methanol molecules strongly interact *via* hydrogen bonding with the triazole rings d[N5···O1] = 2.794 Å and are involved in two short contacts, d[O1···H5] = 2.485 Å and d[O1···H3] = 2.401 Å, with the pyridine and pyrazole rings, respectively of adjacent chains belonging to the same layer (Fig. 6a). An additional short contact, d[H1···N6] = 2.362 Å takes place between the pyrazole and triazole rings, respectively of the adjacent chains belonging to the same layer (Fig. 6b). Consequently, in a layer all complexes are interconnected through a dense network of short supramolecular interactions. In contrast, no relevant contacts occur between molecules belonging to two adjacent layers which stack along *c*.

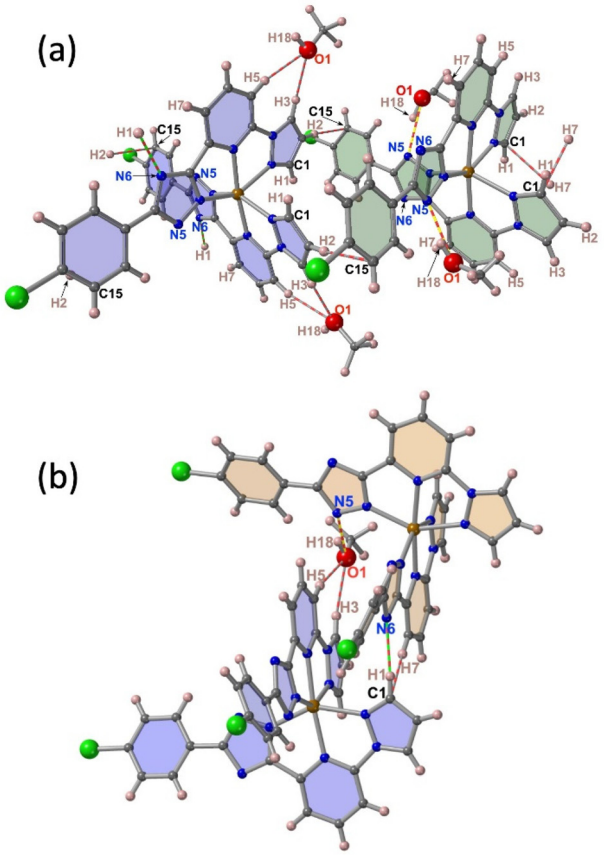

Fig. 6 Intermolecular interactions within the same column (a) and between adjacent columns of the same layer (b) of **4Cl**·2MeOH (for simplicity only one of two interactions filling the rectangular void).

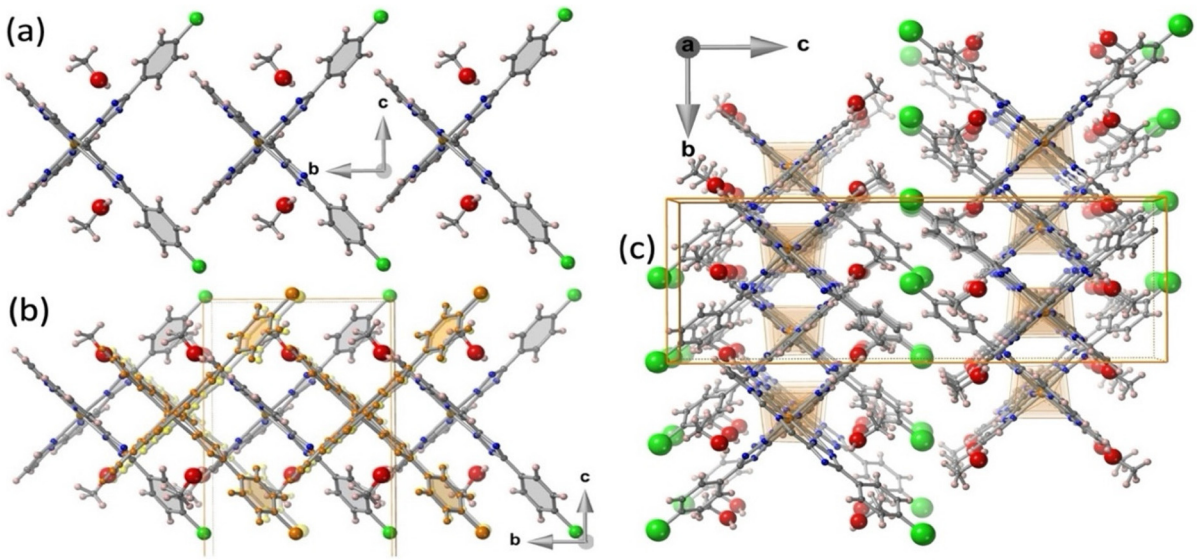

Fig. 5 Crystal packing of **4Cl**·2MeOH: (a) Three consecutive molecules defining a column along *b*-axis. (b) superposition along *a* of two adjacent 1D columns, shifted *b*/2 relatively to each other. (c) Unit cell showing the stacking along *c* two adjacent layers laying parallel to the *a*–*b* planes.

Structure of 4Cl. The structure of the desolvated compound was refined by Rietveld analysis from high-quality powder X-ray diffraction data obtained for both, HS and LS states, at 290 and 100 K, respectively (see Fig. S8†). The loss of the two methanol molecules takes place without change of space group, which is retained whatever the spin state adopted by the Fe(II) centres. The corresponding structural parameters are in Table S3† and selected bond-lengths, angles and geometrical parameters of the coordination core for the HS/LS structures are gathered in Table 1. Upon desolvation, the most remarkable structural change is observed in *c* parameter (HS), which decreases by 11.07%. Furthermore, an additional decrease in *c* of 13.32% occurs upon HS-to-LS transformation. In terms of unit cell volume variation corresponds to ΔV^{HS-LS} = 63.91 Å^3 (Z = 4). The obtained $\langle Fe-N\rangle^{av}/\Phi/\Theta/\alpha/\beta$ parameters, 2.202 Å/150.4°/390°/100.1°/23.1° and 1.932 Å/101.3°/292°/85.8°/10.9° are consistent with the HS and LS states, respectively, in perfect agreement with the magnetic properties. It is relevant to remark the important synchronized scissor-like movement experienced by the two ligands wrapping the Fe^{II} centres, $\Delta\alpha^{HS-LS}$ = 14.3°, and the simultaneous rotation of the phenyl group, $\Delta\beta^{HS-LS}$ = 12.2°, when moving from the HS to the LS state (see Fig. 7a). Obviously, these intramolecular changes have an important impact in the intermolecular interactions and hence in the cooperativity.

The supramolecular organization of the desolvated form is very similar to that of the solvated one (Fig. S9†). However, the molecules belonging to adjacent layers are now much more packed in *c*-direction, for the desolvated form. In the HS state, there are two short contacts between the pyrazole and 4Cl-ph (tail) rings of consecutive molecules within the columns [*d*(H2···C11/C15/C16) = 2.846/2.845/2.736 Å]. Similarly, the short contact between the pyrazole and triazole rings of two molecules of adjacent chains belonging to the same layer [*d*(H3···N5) = 2.401 Å] is also observed. However, both types of contacts are slightly more relaxed than those observed for the solvated compound. Despite this, as expected, the short contacts increase in number in the LS state. For example, between the pyrazole and 4Cl-Ph (tail) rings in the same column (*d* [H2···C12/C13/14/15] = 2.868/2.664/2.612/2.790 Å) and in adjacent columns *d*[C3···H12 = 2.549 Å]; *d*(N3···H3/H5) = 2.480/2.685 Å but they are not substantially shorter than those observed for the solvated species (Fig. 7b–d). Table S4† contains detailed information about supramolecular contacts for the desolvated form.

Energy framework analysis

Energy framework analysis is a convenient visual tool for analyzing the interaction energy within molecular crystal structures and correlating with the ST properties arising from these

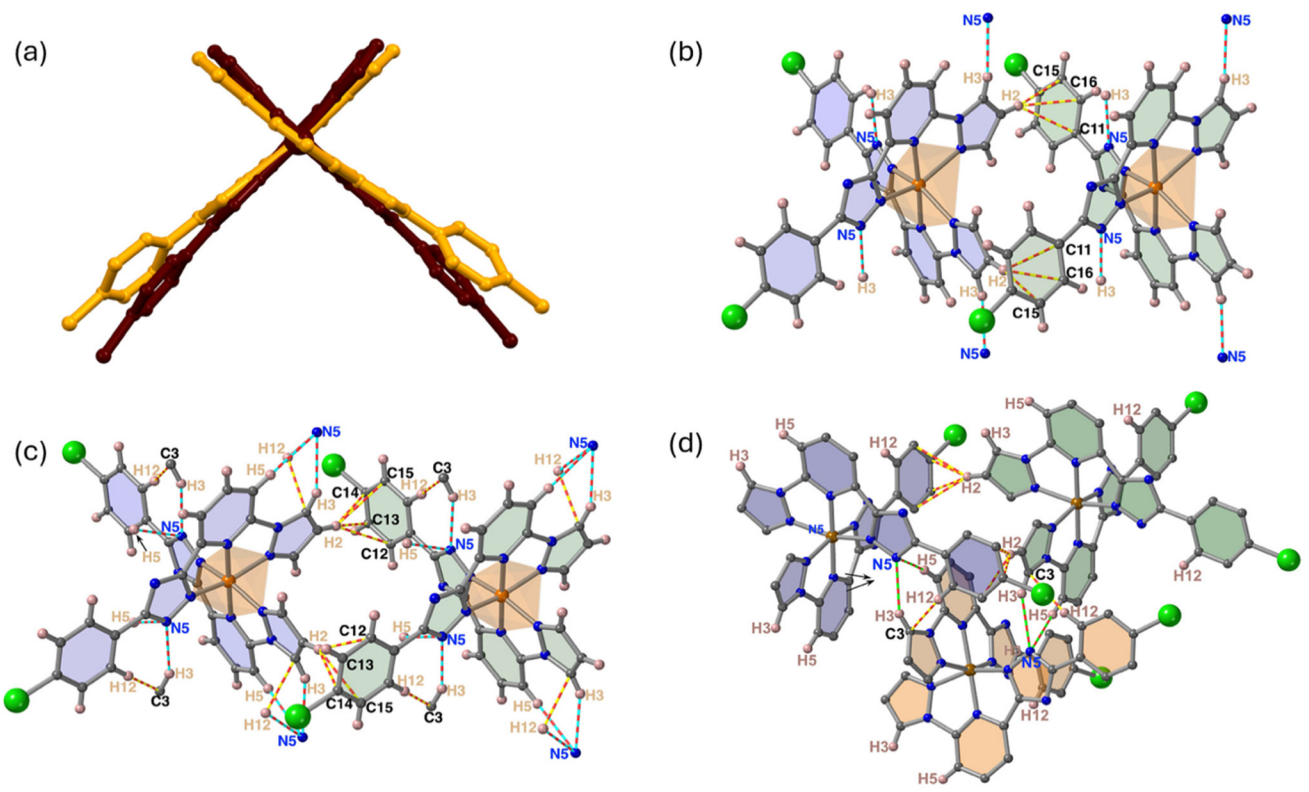

Fig. 7 (a) Minimized overlay showing structural changes due to the ST between the LS (brown) and HS (orange) spin states of the **4Cl** molecule; (b) and (c) Intermolecular interactions between two consecutive molecules of the same column in the HS and LS states, respectively, and (d) between two consecutive molecules of adjacent chains.

structures.[27] The method assumes the representation of intermolecular interactions in the form of cylindrical bonds between the centroids of neighboring molecules, the radius of the cylinder being proportional to the value of the interaction energy, which takes into account the contributions of electrostatic, polarization, dispersion and exchange-repulsion interactions calculated by quantum mechanical methods on the basis of a suitable molecular wave functions. Initially created as a tool to understand the mechanical properties of crystals, energy framework analysis has found its application in ST research as well for understanding structural changes and resulting ST behavior.

A further development of the method is the analysis of the energy difference framework (EDF) calculated for the framework in the LS and HS states. This allows the mapping of changes in interactions with the immediate neighbors, considering the full set of intermolecular interactions. This contrasts with the classical approach, which considers only the strongest interaction below van der Waals radii. The EDF enables identification of the molecule-molecule contacts that is the most affected on transformation and provides insight into the pathways of the ST cooperativity.[19,20,28] The constructed EDF of **4Cl**, calculated using B3LYP/6-31G(d,p) wavefunction, features a three-dimensional character, with larger amplitudes of stabilizing (negative, in the range −0.9 to −7.9 kJ mol^{-1}) intermolecular changes localized within the supramolecular layers formed by stacking molecules and destabilizing (positive, 6.7 kJ mol^{-1}) changes localized between the layers (Fig. 8 and Table S5†). The simultaneous presence of significant stabilizing and destabilizing lattice energy changes is attributed to more cooperative ST transitions, whereas smaller changes are associated with less cooperative ST transitions as it was demonstrated in reported studies.[19,20,28,29] Correspondingly, the hysteretic behavior of **4Cl** is attributed to the presence of balanced energy changes of opposite sign.

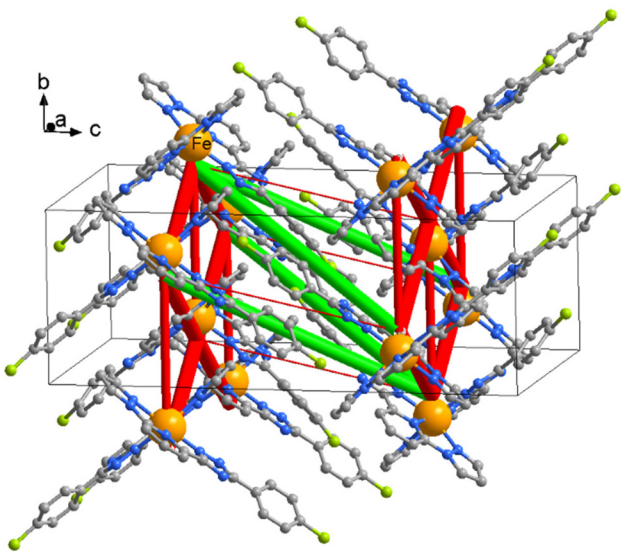

Fig. 8 A fragment of the crystal packing of **4Cl** in the HS state superimposed on the differential energy framework, constructed using the values from the Table S5,† column "Δ*E*(total)(HS−LS)", showing negative intra-layer energetics (red cylinders) and positive inter-layer energetics (green cylinders) due to the lattice changes during the ST event. Cylinder thickness is proportional to the absolute value of the interaction energy.

Photoluminescence emission

The temperature dependence of the photoluminescence emission spectra of **4Cl** has been recorded under a LED excitation of 275 nm (0.8 μW mm^{-2}) in the heating and cooling modes with a scan rate of 5 K min^{-1}. Fig. 9a displays the evolution of the emission spectra in the wave-length interval 300–800 nm in the heating mode. At 200 K, in the LS state, three different bands appear at 396, 530 and 610 nm. Upon heating, the intensity of these bands decreases due to thermal quenching until *ca.* 300 K. From around 300 to 350 K the luminescence increases to decrease again from 350 K. This unexpected increase of the emission bands near the temperature interval where the ST takes place in the heating mode has been previously related to the lower absorption properties of the ST compound in the HS state in the visible range (Fig. 9a).[2c,d,g,4i,5c,13a,b,d,30] In the cooling mode, the same phenomenon is observed: the photoluminescence signal is recovered when decreasing the temperature as thermal quenching is reduced except in the 100–200 K. This is again associated to the ST taking place during cooling in that temperature interval and the ensuing recover of the LS state d–d absorption bands in the visible range which overlap with the emission. The thermal dependence of the normalized photoluminescence intensity in the heating mode shows a reasonably good agreement with that of the HS molar fraction obtained from magnetism (Fig. 9b). However, in the cooling mode, although the intensity of the photoluminescence starts to decline once the LS state attains 100% population (cooling branch of the hysteresis), the results differ significantly.

In addition to the intensity change, it is worth noticing that the thermal evolution of the fluorescence spectra shows a shift of the maxima towards higher/lower energies upon cooling/heating, which takes place only during the ST (see Fig. 9a). This is also illustrated in Fig. S10† where an enlarged representation of the emission thermal dependence for the heating and cooling modes in the 380–500 nm interval is shown. The thermal variation of the wavelength maximum at 440–390 nm, shown in Fig. 10, features very similar characteristic temperatures to those observed for the intensity change (Fig. 9b), although in the former case the transition is more abrupt. The change in radiation can be observed with the naked eye, as shown in Fig. 10, and is bistable at RT in accordance with the ST bistability of the compound.

Discussion

Here we have investigated a new neutral mononuclear $[Fe^{II}(L)_2]^0$ complex with L being a ionogenic tridentate ligand based on the R-(4*H*-1,2,4-triazol-3-yl)-6-(1*H*-pyrazol-1-yl)pyri-

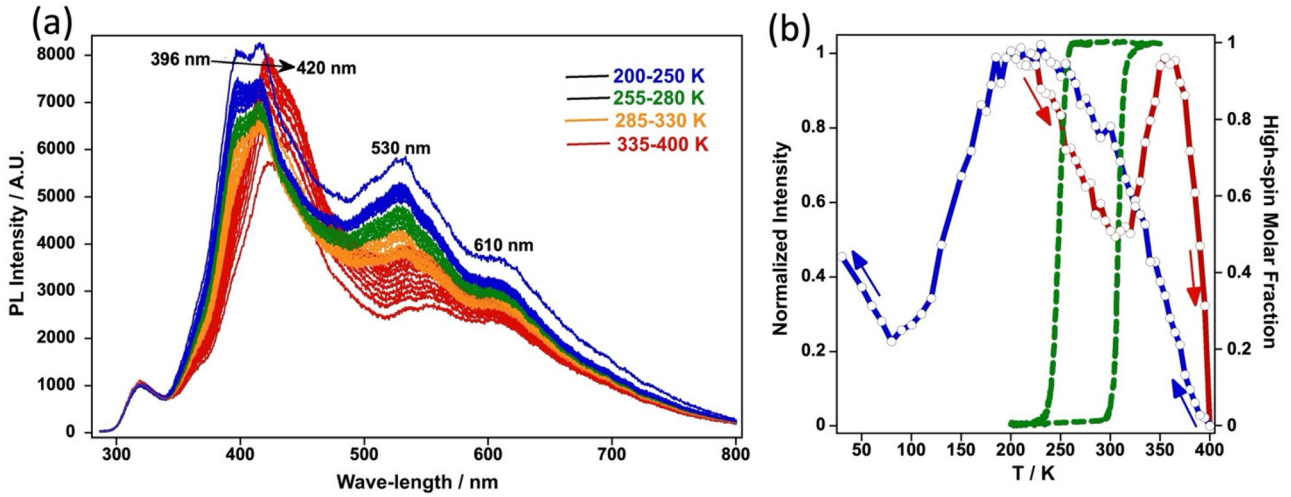

Fig. 9 Temperature evolution of the photoluminescence emission spectra in the heating mode (a) and correlation of the emission intensity in the cooling (blue) and heating (red) modes measured at 420 nm with the HS state population (green) (b) for **4Cl**.

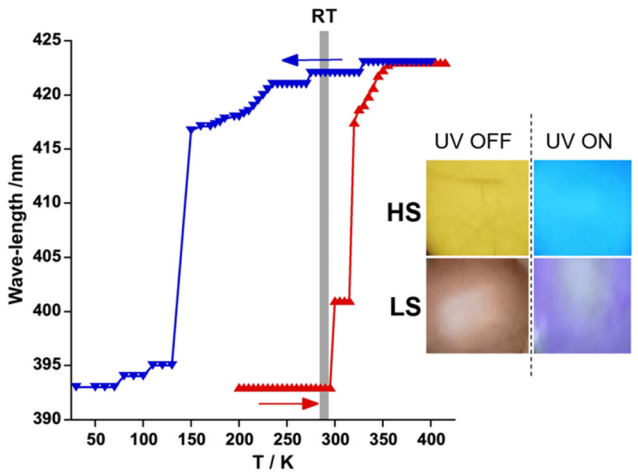

Fig. 10 Temperature dependence of the 440–390 nm band maximum for **4Cl**. The photographs of a sample demonstrate distinct coloration and emission colors corresponding to the two spin states at RT.

dine donor core and R is the peripheral substituent 4-chlorophenyl. Its methanolate form, **4Cl**·2MeOH, is HS at all temperatures, a fact that strongly contrasts with the homologous solvates of the two first members of this family of compounds, which differing in R = 2-(5-(3-methoxyphenyl)) (**3MeO**·2MeOH) or 2-(5-(2-fluorophenyl)) (**2F**·2MeOH), display ST behaviour near room temperature.[19,20] At first sight, this fact can contradict with the remarkable similarity of their crystal packing. However, it is well known that the lack or presence of ST critically depends on subtle structural and electronic differences in the crystal packing due to, among others, by polymorphic variants, solvents, counterions or, as in the present case, by a R substituent in the organic ligand. In the present case, the Cl substituent located in 4-position of the peripheral phenyl moiety seems to favour the much tighter packing between the molecules of the same layer, a fact that locks the HS state in **4Cl**·2MeOH, since the switch to the LS state, which is prevented in this case, is usually accompanied by an even closer packing of the molecules. The loss of the methanol molecules seems to relax the crystal packing, a fact reflected on the trigonal distortion of the coordination octahedron, Θ, which decreases by *ca.* 20% for the HS state of the desolvated **4Cl**. Despite this, the α angle defined by the two independent pyridine-triazole-pyrazole cores, attached around the Fe^{II} ion, increases almost 8% for the HS state in **4Cl** with respect to that of the methanolate form. Upon HS → LS change, the characteristic scissor-like movement, $\Delta\alpha^{HS-LS}$, involves a decrease of 14.3°, which is around 7–10 times larger than that found for the complexes **2F**·2MeOH and the not annealed desolvated phase of **3MeO** (phase 1B). This structural modification could be the reason of the much wider hysteresis loop observed for **4Cl**. In this respect, it deserves to be mentioned that the annealed phase of the fully desolvated **3MeO** (phase 1C) features a negative $\Delta\alpha^{HS-LS} = -8.3°$ with $\alpha^{HS} = 76.9°$, markedly smaller than $\alpha^{LS} = 85.2°$. This opposite behaviour in $\Delta\alpha^{HS-LS}$ has been rationalized by an additional concurrent lock-unlock "latch-like" mechanism induced by the extended-bent flipping conformations of the group MeO-ph which favours the occurrence of a 105 K wide hysteresis loop exhibited by **3MeO** (phase 1C).[19]

The T_c^{av} values obtained from magnetism, optical density measurements, and calorimetry are perfectly consistent. However, the maximum/minimum of ΔCp in the cooling/warming modes take place just at the onset of the sharp decrease/increase in $\chi_M T$ giving an apparent hysteresis 20 K narrower, however, it is important to remark that the hysteresis is well reproduced when considering the temperatures at which ΔC_p joins the zero value in the cooling and heating modes, namely, when the total heat required by the ST has come into play (Fig. S7†).

Due to thermal quenching, the fluorescence emission of **4Cl** decreases/increases markedly as temperature increases/decreases in the temperature range 15–400 K. However, this general monotonous behaviour is interrupted by the ST event in a different fashion depending on what spin state is being populated (Fig. 9). Thus, in the heating mode, the fluorescence emission starts to increase from 300 K and reaches a relative maximum at ca. 350 K once the LS → HS transition is completed. The characteristic temperatures at which this emission increase takes place, display a small mismatch with respect to the thermal dependence of HS molar fraction deduced from the magnetic behaviour in the heating mode. In the cooling mode, the emission starts to gradually decrease from ca. 250 K, the onset of the HS → LS transition according to the magnetic properties, but this decrease extends to a much wider temperature interval and attains a minimum at ca. 100 K making the mismatch with the corresponding HS molar fraction much larger. This behaviour is also reflected on the bathochromic/hypsochromic shift of the fluorescence maximum at 390–430 nm upon heating/cooling. A possible explanation for this behaviour relies on two concurrent opposite effects taking place over the fluorescence emission: on one hand, it decreases with the increase of the LS population upon cooling but, on the other hand, it tends to simultaneously increase as the temperature decreases, thereby resulting in the apparent progressive thermal delay of the HS → LS event upon cooling. An equivalent effect should be expected for the LS → HS event in the heating mode, but it seems to be significantly smaller as the thermal delay is much smaller. In this respect, marked differences between the characteristic ST temperature and that at which the change of photoluminescence takes place, have been recently reported. For example, the mononuclear compound $(Fe(L)_2)(ClO_4)_2$ (L is a pyridinecarbaldehyde rhodamine 6G hydrazone ligand) displays, upon heating, an abrupt ST at T_c^{up} = 343 K, while *ca.* 70% of the associated photoluminescence increase takes place gradually bellow this temperature in the interval 300–343 K.[4i] The opposite occurs for the octanuclear cage $(Fe_8L_6)(BF_4)_{16}{\cdot}CH_3OH$ (L = *N*-(ethene-1,1,2,2-tetrayltetrakis(benzene-4,1-diyl))tetrakis(1-(1*H*-imidazol-4-yl)methanimine) which undergoes a quite symmetric and relatively gradual ST in the temperature interval 250–150 K with $T_{1/2} \approx 190$ K. For this compound the increase of PL associated with the population of the HS state is shifted *ca.* 60 K above $T_{1/2}$.[13b] A similar behavior has been observed for compounds $[Fe(tpe\text{-}abpt)_2(SeCN)_2]{\cdot}4DMF$ (tpe-abpt: (4-(1,1,2,2-tetraphenylethene))-*N*-(3,5-bis(pyridin-2-yl)-4*H*-1,2,4-triazol-4yl) methanimine)),[30b] $[Fe^{II}(BPND)\{Ag(CN)_2\}_2]{\cdot}3CHCl_3$ (BPND = *N*,*N*′-bis(4-pyridylmethyl)-1,4,5,8-naphthalene diimide)[30c] and $[Fe^{II}(tppe)Au(CN)_2]ClO_4{\cdot}n$Solv (tppe = tetra-(4-pyridylphenyl) ethene).[13d]

Furthermore, as the measurements were conducted under continuous irradiation, we cannot rule out the possibility of local heating of the sample. Magnetic measurements performed in darkness or under microscope lamp for optical density measurements reveal the same intrinsic behavior with identical position and width of the ST hysteresis. However, when subjected to high energy irradiation (UV for the fluorescence) or laser beam exposure (green laser for Raman scattering), significant modulation of the loop is observed. In this respect, the literature describes a light-induced perturbation of thermal hysteresis (LiPTH), which shifts the ST towards lower temperatures. This phenomenon, characterized by Mössbauer spectroscopy on a bulk sample[31] and optically on single crystals,[32] was attributed to photothermal heating, whereby the compound absorbs light, generating local heat altering the actual temperature of the sample. It is evident that the surface of the sample experiences the greatest impact, and namely the surface response is registered using the fluorescence method. We believe that both the change in absorption and the surface heating effect contribute to the HS fluorescence response. This results in an initially continuous transition, followed by a sharp drop to the LS upon cooling, accompanied by a significant thermal lag compared to the magnetic/optical response. At higher temperature, where the reverse transition to the HS state occurs, the system exhibits minimal impact from irradiation. Worth to note, in a recent publication on two-dimensional ST metal–organic frameworks $[Fe^{II}(PNI)_2\{Ag(CN)_2\}_2]$ (PNI = *N*-(4-pyridylmethyl)-1,8-naphthalimide) with 40 K wide ST a similar lag in fluorescent signal variation on cooling is reported, while absent on heating.[13c] This behavior may suggest a nonlinear change in effect across the temperature range, warranting further investigation with compounds with huge hysteresis as the reports on the LiPTH focused on compounds with thermal loops 10 K wide.[31,32]

In summary, a new neutral mononuclear complex incorporating a pyrazole-pyridine-triazole coordination core has been synthesized. In its desolvated form, the complex exhibits highly cooperative ST behavior with a hysteresis 60 K wide loop. Concurrently, the complex displays room-temperature two colored fluorescence, directly correlated with the ST state. To the best of our knowledge, this represents the first instance of a ST compound exhibiting hysteretic thermochromism and bistable correlated fluorescence properties encompassing room temperature. The additional readout channel provided by the fluorescent response under UV irradiation offers a promising avenue for developing novel fluorescent probes capable of detecting and quantifying changes in temperature, pressure, or the presence of specific analytes that can induce a spin state transition. Studies of novel ST-fluorescent systems are currently ongoing in our laboratories, and the results will be presented in due course.

Experimental section

Materials

All chemicals and solvents were purchased from commercial sources and used without further purification. The ligand L was synthesized by the Suzuki cross-coupling reaction from the commercially available precursors similarly to the previously reported method.[19]

Synthesis of complexes

4Cl·2MeOH ([FeL_2]·2MeOH) was produced by layering in standard test tube. The layering sequence was as follows: the bottom layer contains a solution of [FeL_2](BF_4)$_2$ prepared by dissolving L (100 mg, 0.310 mmol) and $Fe(BF_4)_2{\cdot}6H_2O$ (52 mg, 0.160 mmol) in boiling acetone, to which chloroform (5 ml) was then added. The middle layer was a methanol–chloroform mixture (1 : 10) (10 ml) which was covered by a layer of methanol (10 ml), to which 100 μl of NEt_3 was added dropwise. The tube was sealed, and yellow plate-like single crystals appeared in 2 weeks (yield *ca.* 70%). Elemental analysis calcd for $C_{34}H_{28}Cl_2FeN_{12}O_2$: C, 53.49; H, 3.70; N, 22.02. Found: C, 53.54; H, 3.81; N, 22.73.

4Cl ([FeL_2]) was prepared by a short heating **4Cl**·2MeOH up to 400 K or by leaving the crystalline sample in air for 30 minutes. Elemental analysis calcd for $C_{32}H_{20}Cl_2FeN_{12}$: C, 54.96; H, 2.88; N, 24.03. Found: C, 54.71; H, 2.54; N, 24.38.

Physical characterization

Variable-temperature magnetic susceptibility data (15–20 mg) were recorded on samples at variable rates between 10–400 K using a Quantum Design MPMS2 SQUID susceptometer operating at 1 T magnet. The LIESST experiments were performed at 10 K in a commercial sample holder (Quantum Design Fiber Optic Sample Holder), wherein a quartz bucket containing *ca.* 1 mg of a sample was held against the end of a quartz fiber coupled with a red laser (633 nm, 15 mW cm^{-1}). After reaching the saturation of susceptibility, the sample was heated up at the rate 0.3 K min^{-1}. The raw data were corrected for a diamagnetic background arising from the sample holder. The resulting magnetic signal was calibrated by scaling to match values with those of bulk sample. Differential scanning calorimetric (DSC) measurements were performed on a Mettler Toledo TGA/SDTA 821e under a nitrogen atmosphere with a rate of 10 K min^{-1}. The raw data were analyzed with the Netzsch Proteus software with an overall accuracy of 0.2 K in the temperature and 2% in the heat flow. Thermogravimetric analysis (TGA) was performed on a Mettler Toledo TGA/SDTA 851e instrument, in the 290–1200 K temperature range under a nitrogen atmosphere at a rate of 10 K min^{-1}. Elemental CHN analysis was performed after combustion at 850 °C using IR detection and gravimetry by means of a Perkin–Elmer 2400 series II device. Single crystal X-ray diffraction data of 2F were collected on a Nonius Kappa-CCD single crystal diffractometer using graphite mono-chromated Mo K_α radiation (λ = 0.71073 Å). A multi-scan absorption correction was performed. The structures were solved by direct methods using SHELXS-2014 and refined by full-matrix least squares on F^2 using SHELXL-2014.[33] Non-hydrogen atoms were refined anisotropically and hydrogen atoms were placed in calculated positions refined using idealized geometries (riding model) and assigned fixed isotropic displacement parameters. The system for monitoring the ST by optical reflectance consisted of a LINKAM DSC600 thermal stage operating at 5 K min^{-1} scan rate, a binocular microscope with a digital camera. Image processing was performed using ImageJ software. Raman spectra were recorded at 293 K using a HORIBA LabRAM HR Evolution equipped with a laser beam with adjustable wavelength and power and a 50× lens to focus the beam and a LINKAM DSC600 thermal stage. The bulk material was placed directly on a glass slide and measured. All spectra, collected between 100 cm^{-1} and 1800 cm^{-1}, were normalized to facilitate their comparison.

High resolution powder X-ray diffraction patterns were collected at room temperature, at the I11 beamline of the Diamond Light Source synchrotron (UK), using a wavelength of 0.826844 Å. The sample was loaded into a borosilicate capillary and mounted on a spinning goniometric head, to reduce the possible preferential orientation effects. Measurements were performed in a 2θ continuous scan mode, in a 0.001° step size, using the multi-analysing crystal (MAC) device. Raw data was acquired within a 0–150° 2θ range, although the final refined ranges were 2.75–47°, corresponding to a resolution of 1.03 Å. The crystal structures of 4Cl(LS) and 4Cl(HS) were solved and refined by means of the Rietveld method using Topas Academic 6 software (**https://www.topas-academic.net/**). Final Rietveld plots are given in Fig. S8,† while crystallographic and refinement parameters are summarized in Table S3.†

CCDC files, 2424238 (**4Cl**·2MeOH), 2416066 (**4Cl**, HS) and 2416064 (**4Cl**, LS)† contain the supplementary crystallographic data for this paper.

Author contributions

Conceptualization: M. S.; experimental investigation: M. S., K. Z.; instrumental measurements and formal analysis: M. S., K. Z., F. J. V.-M., M. C. M., T. D. and I. daS.; data processing and visualization: M. S., K. Z. and J. A. R.; writing of the original draft: M. S., K. Z. and J. A. R.; writing – review & editing: all authors; supervision, project administration, and funding acquisition: M. S. and J. A. R. The manuscript was written through contributions of all the authors. All authors have given approval to the final version of the manuscript.

Data availability

The data supporting this article have been included as part of the ESI.† Crystallographic data for **4Cl**·2MeOH and **4Cl** (HS and LS) have been deposited at The Cambridge Crystallographic Data Centre with CCDC numbers 2424238 (**4Cl**·2MeOH), 2416066 (**4Cl**, HS) and 2416064 (**4Cl**, LS).†

Conflicts of interest

There are no conflicts to declare.

Acknowledgements

This work was supported by the Spanish Ministerio de Ciencia, Innovación y Universidades [(MICIU/AEI/10.13039/

501100011033) and FEDER/UE, through grant PID2023-150732NB-I00 and María de Maeztu (CEX2024-001467-M), and Ministry of Education and Science of Ukraine (24BF037-03). This project has received funding from the European Union's Horizon 2020 research and innovation programme under the Marie Skłodowska-Curie grant agreement No. 899546. Dr I. Gural'sky is acknowledged for preliminary optical reflectance measurements. T.D. thanks the Swiss Naeonal Science Foundaeon for financial support through grant Postdoct. Mobility P400P2_191108/1.

References

1 (*a*) E. König, Nature and dynamics of the spin-state interconversion in metal complexes, *Struct. Bonding*, 1991, **76**, 51–152; (*b*) P. Gütlich, A. Hauser and H. Spiering, Thermal and optical switching of iron(II) complexes, *Angew. Chem., Int. Ed. Engl.*, 1994, **33**, 2024–2054; (*c*) J. A. Real, A. B. Gaspar, V. Niel and M. C. Muñoz, Communication between iron(II) building blocks in cooperative spin transition phenomena, *Coord. Chem. Rev.*, 2003, **236**, 121–141; (*d*) Spin crossover in transition metal compounds I-III, in *Top. Curr. Chem*, ed. P. Gütlich and G. Goodwin, 2004, vol. 233–235; (*e*) J. A. Real, A. B. Gaspar and M. C. Muñoz, Thermal, pressure and light switchable spin-crossover materials, *Dalton Trans.*, 2005, 2062–2079; (*f*) C. T. Brewer, G. Brewer, R. J. Butcher, E. E. Carpenter, A. M. Schmiedekamp and C. Viragh, Synthesis and characterization of a spin crossover iron(II)-iron(III) mixed valence supramolecular pseudo-dimer exhibiting chiral recognition, hydrogen bonding, and pi-pi interactions, *Dalton Trans.*, 2007, 295–298; (*g*) Y. Sunatsuki, R. Kawamoto, K. Fujita, H. Maruyama, T. Suzuki, H. Ishida, M. Kojima, S. Iijima and N. Matsumoto, Structures and spin states of mono- and dinuclear iron(II) complexes of imidazole-4-carbaldehyde azine and its derivatives, *Coord. Chem. Rev.*, 2010, **254**, 1871–1881; (*h*) M. C. Muñoz and J. A. Real, Thermo-, piezo-, photo- and chemo-switchable spin crossover iron(II)-metallocyanate based coordination polymers, *Coord. Chem. Rev.*, 2011, **255**, 2068–2093; (*i*) G. Aromí, L. A. Barrios, O. Roubeau and P. Gamez, Triazoles and tetrazoles: Prime ligands to generate remarkable coordination materials, *Coord. Chem. Rev.*, 2011, **255**, 485–546; (*j*) R. W. Hogue, S. Singh and S. Brooker, Spin crossover in discrete polynuclear iron(II) complexes, *Chem. Soc. Rev.*, 2018, **47**, 7303–7338; (*k*) Spin crossover phenomenon, in *C. R. Chimie*, ed. A. Bousseksou, 2018, vol. 21, pp. 1055–1299.

2 (*a*) O. Kahn and J. Martinez, Spin-transition polymers: From molecular materials toward memory devices, *Science*, 1998, **279**, 44–48; (*b*) J. F. Létard, P. Guionneau and L. Goux-Capes, Towards spin crossover applications, *Top. Curr. Chem.*, 2004, **235**, 221–249; (*c*) Y. Garcia, F. Robert, A. D. Naik, G. Zhou, B. Tinant, K. Robeyns, S. Michotte and L. Piraux, Spin Transition Charted in a Fluorophore-Tagged Thermochromic Dinuclear Iron(II) Complex, *J. Am. Chem. Soc.*, 2011, **133**, 15850–15853; (*d*) H. J. Shepherd, C. M. Quintero, G. Molnár, L. Salmon and A. Bousseksou, in *Spin-Crossover Materials*, John Wiley & Sons Ltd, 2013, pp. 347–373; (*e*) M. D. Manrique-Juarez, S. Rat, L. Salmon, G. Molnar, C. M. Quintero, L. Nicu, H. J. Shepherd and A. Bousseksou, Switchable molecule-based materials for micro- and nanoscale actuating applications: Achievements and prospects, *Coord. Chem. Rev.*, 2016, **308**, 395–408; (*f*) G. Molnár, S. Rat, L. Salmon, W. Nicolazzi and A. Bousseksou, Spin Crossover Nanomaterials: From Fundamental Concepts to Devices, *Adv. Mater.*, 2018, **30**, 1703862; (*g*) T. Delgado, M. Meneses-Sanchez, L. Pineiro-Lopez, C. Bartual-Murgui, M. C. Muñoz and J. A. Real, Thermo- and photo-modulation of exciplex fluorescence in a 3D spin crossover Hofmann-type coordination polymer, *Chem. Sci.*, 2018, **9**, 8446–8452; (*h*) K. S. Kumar and M. Ruben, Sublimable Spin-Crossover Complexes: From Spin-State Switching to Molecular Devices, *Angew. Chem., Int. Ed.*, 2021, **60**, 7502–7521; (*i*) E. Resines-Urien, M. Á. G. García-Tuñón, M. García-Hernández, J. A. Rodríguez-Velamazán, A. Espinosa and J. S. Costa, Concomitant Thermochromic and Phase-Change Effect in a Switchable Spin Crossover Material for Efficient Passive Control of Day and Night Temperature Fluctuations, *Adv. Sci.*, 2022, **9**, 2202253; (*j*) R. Torres-Cavanillas, M. Gavara-Edo and E. Coronado, Bistable Spin-Crossover Nanoparticles for Molecular Electronics, *Adv. Mater.*, 2023, **36**, 2307718; (*k*) M. Gavara-Edo, F. J. Valverde-Muñoz, R. Córdoba, M. C. Muñoz, J. Herrero-Martín, J. A. Real and E. Coronado, Sublimable complexes with spin switching: chemical design, processing as thin films and integration in graphene-based devices, *J. Mater. Chem. C*, 2023, **11**, 8107–8120; (*l*) M. Seredyuk, R. Li, K. Znovjyak, Z. Zhang, F. J. Valverde-Muñoz, B. Li, M. C. Muñoz, Q. Li, B. Liu, G. Levchenko and J. A. Real, Reversible Colossal Barocaloric Effect of a New FeII Molecular Complex with Low Hysteretic Spin Crossover Behavior, *Adv. Funct. Mater.*, 2024, 2315487.

3 F. J. Valverde-Muñoz, R. Kazan, K. Boukheddaden, M. Ohba, J. A. Real and T. Delgado, Downsizing of Nanocrystals While Retaining Bistable Spin Crossover Properties in Three-Dimensional Hofmann-Type {Fe(pz)[Pt(CN)$_4$]}-Iodine Adducts, *Inorg. Chem.*, 2021, **60**, 8851–8860.

4 (*a*) Z. J. Zhong, J. Q. Tao, Z. Yu, C. Y. Dun, Y. J. Liu and X. Z. You, A stacking spin-crossover iron(II) compound with a large hysteresis, *J. Chem. Soc., Dalton Trans.*, 1998, **3**, 327–328; (*b*) B. Weber, W. Bauer and J. Obel, An Iron(II) Spin-Crossover Complex with a 70 K Wide Thermal Hysteresis Loop, *Angew. Chem., Int. Ed.*, 2008, **47**, 10098–10101; (*c*) G. A. Craig, J. Sánchez Costa, O. Roubeau, S. J. Teat and G. Aromí, Coupled Crystallographic Order-Disorder and Spin State in a Bistable Molecule: Multiple Transition Dynamics, *Chem. Eur. J.*, 2011, **17**, 3120–3127; (*d*) T. D. Roberts, F. Tuna, T. L. Malkin, C. A. Kilner and M. A. Halcrow, An iron(II) complex exhibiting five anhy-

drous phases, two of which interconvert by spin-crossover with wide hysteresis, *Chem. Sci.*, 2012, **3**, 349; (*e*) M. Seredyuk, M. C. Muñoz, M. Castro, T. Romero-Morcillo, A. B. Gaspar and J. A. Real, Unprecedented multistable spin crossover molecular material with two thermal memory channels, *Chem. – Eur. J.*, 2013, **19**, 6591–6596; (*f*) M. B. Bushuev, V. A. Daletsky, D. P. Pishchur, Y. V. Gatilov, I. V. Korolkov, E. B. Nikolaenkova and V. P. Krivopalov, Unprecedented bistability domain and interplay between spin crossover and polymorphism in a mononuclear iron(II) complex, *Dalton Trans.*, 2014, **43**, 3906; (*g*) E. Tailleur, M. Marchivie, N. Daro, G. Chastanet and P. Guionneau, Thermal spin-crossover with a large hysteresis spanning room temperature in a mononuclear complex, *Chem. Commun.*, 2017, **53**, 4763–4766; (*h*) A. Djemel, O. Stefanczyk, M. Marchivie, E. Trzop, E. Collet, C. Desplanches, R. Delimi and G. Chastanet, Solvatomorphism-Induced 45 K Hysteresis Width in a Spin-Crossover Mononuclear Compound, *Chem. – Eur. J.*, 2018, **24**, 14760–14767; (*i*) J. Yuan, S.-Q. Wu, M.-J. Liu, O. Sato and H.-Z. Kou, Rhodamine 6G-Labeled Pyridyl Aroylhydrazone Fe(II) Complex Exhibiting Synergetic Spin Crossover and Fluorescence, *J. Am. Chem. Soc.*, 2018, **140**, 9426–9433; (*j*) K. Senthil Kumar, B. Heinrich, S. Vela, E. Moreno-Pineda, C. Bailly and M. Ruben, Bi-stable spin-crossover characteristics of a highly distorted [Fe(1-BPP-$COOC_2H_5)_2$]$(ClO_4)_2$·CH_3CN complex, *Dalton Trans.*, 2019, **48**, 3825–3830; (*k*) N. Suryadevara, A. Mizuno, L. Spieker, S. Salamon, S. Sleziona, A. Maas, E. Pollmann, B. Heinrich, M. Schleberger, H. Wende, S. K. Kuppusamy and M. Ruben, Structural insights into hysteretic spin-crossover in a set of iron(II)-2,6-bis(1*H*-pyrazol-1-yl)pyridine) complexes, *Chem. – Eur. J.*, 2022, **28**, e202103853.

5 (*a*) F. J. Muñoz Lara, A. B. Gaspar, D. Aravena, E. Ruiz, M. C. Muñoz, M. Ohba, R. Ohtani, S. Kitagawa and J. A. Real, Enhanced bistability by guest inclusion in Fe(II) spin crossover porous coordination polymers, *Chem. Commun.*, 2012, **48**, 4686–4688; (*b*) M. M. Dirtu, A. D. Naik, A. Rotaru, L. Spinu, D. Poelman and Y. Garcia, Fe-II Spin Transition Materials Including an Amino-Ester 1,2,4-Triazole Derivative, Operating at, below, and above Room Temperature, *Inorg. Chem.*, 2016, **55**, 4278–4295; (*c*) C. Lochenie, K. Schotz, F. Panzer, H. Kurz, B. Maier, F. Puchtler, S. Agarwal, A. Kohler and B. Weber, Spin-Crossover Iron(II) Coordination Polymer with Fluorescent Properties: Correlation between Emission Properties and Spin State, *J. Am. Chem. Soc.*, 2018, **140**, 700–709; (*d*) M. Grzywa, R. Röß-Ohlenroth, C. Muschielok, H. Oberhofer, A. Błachowski, J. Żukrowski, D. Vieweg, H.-A. K. von Nidda and D. Volkmer, Cooperative Large-Hysteresis Spin-Crossover Transition in the Iron(II) Triazolate $[Fe(ta)_2]$ Metal–Organic Framework, *Inorg. Chem.*, 2020, **59**, 10501–10511; (*e*) A. B. Andreeva, K. N. Le, K. Kadota, S. Horike, C. H. Hendon and C. K. Brozek, Cooperativity and Metal–Linker Dynamics in Spin Crossover Framework Fe(1,2,3-triazolate)$_2$, *Chem. Mater.*, 2021, **33**, 8534–8545.

6 F. Lai, L. Getzner, A. Rotaru, G. Molnár, S. Cobo and A. Bousseksou, Drastic Enhancement of Electrical Conductivity of Metal–Organic Frameworks Displaying Spin Crossover, *Chem. Mater.*, 2025, **37**, 636–643.

7 L. Zhao, Y.-S. Meng, Q. Liu, O. Sato, Q. Shi, H. Oshio and T. Liu, Switching the magnetic hysteresis of an [FeII–NC–WV]-based coordination polymer by photoinduced reversible spin crossover, *Nat. Chem.*, 2021, **13**, 698–704.

8 (*a*) S. Bonhommeau, P. G. Lacroix, D. Talaga, A. Bousseksou, M. Seredyuk, I. O. Fritsky and V. Rodriguez, Magnetism and molecular nonlinear optical second-order response meet in a spin crossover complex, *J. Phys. Chem. C*, 2012, **116**, 11251–11255; (*b*) T. Charytanowicz, K. Dziedzic-Kocurek, K. Kumar, S.-i. Ohkoshi, S. Chorazy and B. Sieklucka, Chirality and Spin Crossover in Iron(II)–Octacyanidorhenate(V) Coordination Polymers Induced by the Pyridine-Based Ligand's Positional Isomer, *Cryst. Growth Des.*, 2023, **23**, 4052–4064.

9 M. K. Javed, A. Sulaiman, M. Yamashita and Z.-Y. Li, Shedding light on bifunctional luminescent spin crossover materials, *Coord. Chem. Rev.*, 2022, **467**, 214625.

10 K. Sun, J.-P. Xue, Z.-S. Yao and J. Tao, Synergistic strategies for the synthesis of Fe(II)-based bifunctional fluorescent spin-crossover materials, *Dalton Trans.*, 2022, **51**, 16044–16054.

11 (*a*) S. Titos-Padilla, J. M. Herrera, X.-W. Chen, J. J. Delgado and E. Colacio, Bifunctional Hybrid SiO_2 Nanoparticles Showing Synergy between Core Spin Crossover and Shell Luminescence Properties, *Angew. Chem., Int. Ed.*, 2011, **50**, 3290–3293; (*b*) J. M. Herrera, S. Titos-Padilla, S. J. A. Pope, I. Berlanga, F. Zamora, J. J. Delgado, K. V. Kamenev, X. Wang, A. Prescimone, E. K. Brechin and E. Colacio, Studies on bifunctional Fe(ii)-triazole spin crossover nanoparticles: time-dependent luminescence, surface grafting and the effect of a silica shell and hydrostatic pressure on the magnetic properties, *J. Mater. Chem. C*, 2015, **3**, 7819–7829.

12 (*a*) M. Matsuda, K. Kiyoshima, R. Uchida, N. Kinoshita and H. Tajima, Characteristics of organic light-emitting devices consisting of dye-doped spin crossover complex films, *Thin Solid Films*, 2013, **531**, 451–453; (*b*) I. Sánchez-Molina, D. Nieto-Castro, A. Moneo-Corcuera, E. Martínez-Ferrero and J. R. Galán-Mascarós, Synergic Bistability between Spin Transition and Fluorescence in Polyfluorene Composites with Spin Crossover Polymers, *J. Phys. Chem. Lett.*, 2021, **12**, 10479–10485.

13 (*a*) M. Meneses-Sánchez, L. Piñeiro-López, T. Delgado, C. Bartual-Murgui, M. C. Muñoz, P. Chakraborty and J. A. Real, Extrinsic vs. intrinsic luminescence and their interplay with spin crossover in 3D Hofmann-type coordination polymers, *J. Mater. Chem. C*, 2020, **8**, 1623–1633; (*b*) R. Turo-Cortés, M. Meneses-Sánchez, T. Delgado, C. Bartual-Murgui, M. C. Muñoz and J. A. Real, Coexistence of luminescence and spin-crossover in 2D iron(II) Hofmann clathrates modulated through guest encapsulation, *J. Mater. Chem. C*, 2022, **10**, 10686–10698; (*c*) X.-R. Wu,

S.-Q. Wu, Z.-K. Liu, M.-X. Chen, J. Tao, O. Sato and H.-Z. Kou, Manipulating guest-responsive spin transition to achieve switchable fluorescence in a Hofmann-type framework, *Sci. China: Chem.*, 2024, **67**, 3339–3346; (*d*) X.-R. Wu, S.-Q. Wu, Z.-K. Liu, M.-X. Chen, J. Tao, O. Sato and H.-Z. Kou, Integrating spin-dependent emission and dielectric switching in FeII catenated metal-organic frameworks, *Nat. Commun.*, 2024, **15**, 3961.

14 M. Hasegawa, F. Renz, T. Hara, Y. Kikuchi, Y. Fukada, J. Okubo, T. Hoshi and W. Linert, Fluorescence spectra of Fe(II) spin crossover complexes with 2,6-bis(benzimidazole-2 '-yl)pyridine, *Chem. Phys.*, 2002, **277**, 21–30.

15 Y. Jiao, J. Zhu, Y. Guo, W. He and Z. Guo, Synergetic effect between spin crossover and luminescence in the $[Fe(bpp)_2][BF_4]_2$ (bpp = 2,6-bis(pyrazol-1-yl)pyridine) complex, *J. Mater. Chem. C*, 2017, **5**, 5214–5222.

16 (*a*) J. L. Wang, Q. Liu, X. J. Lv, R. L. Wang, C. Y. Duan and T. Liu, Magnetic fluorescent bifunctional spin-crossover complexes, *Dalton Trans.*, 2016, **45**, 18552–18558; (*b*) S. Ghosh, S. Kamilya, T. Pramanik, A. Mohanty, M. Rouzières, R. Herchel, S. Mehta and A. Mondal, Thermo- and photoinduced spin state switching in an iron (II) 2D coordination network associated with large light-induced thermal hysteresis and tuning of dimensionality-vialigand modulation, *Dalton Trans.*, 2021, **50**, 7725–7735; (*c*) X. Wang, N. Zhang and H.-Z. Kou, Substituent effects on spin-crossover $Fe(II)N_4O_2$ pyrenylhydrazone complexes, *Dalton Trans.*, 2024, **53**, 16592–16597; (*d*) J. Wu, Q. Yang, X.-L. Li, Z. Zhu, C. Zhao, T. Liu and J. Tang, An AIE-Active Fe(II) Complex Exhibiting Synergistic Spin-Crossover and Luminescent Properties, *Cryst. Growth Des.*, 2025, **25**, 1276–1281.

17 (*a*) R. González-Prieto, B. Fleury, F. Schramm, G. Zoppellaro, R. Chandrasekar, O. Fuhr, S. Lebedkin, M. Kappes and M. Ruben, Tuning the spin-transition properties of pyrene-decorated 2,6-bispyrazolylpyridine based Fe(II) complexes, *Dalton Trans.*, 2011, **40**, 7564–7570; (*b*) M. Estrader, J. Salinas Uber, L. A. Barrios, J. Garcia, P. Lloyd-Williams, O. Roubeau, S. J. Teat and G. Aromí, A Magneto-optical Molecular Device: Interplay of Spin Crossover, Luminescence, Photomagnetism, and Photochromism, *Angew. Chem., Int. Ed.*, 2017, **56**, 15622–15627; (*c*) B. Benaicha, K. Van Do, A. Yangui, N. Pittala, A. Lusson, M. Sy, G. Bouchez, H. Fourati, C. J. Gómez-Garciá, S. Triki and K. Boukheddaden, Interplay between spin-crossover and luminescence in a multifunctional single crystal iron(II) complex: Towards a new generation of molecular sensors, *Chem. Sci.*, 2019, **10**, 6791–6798; (*d*) Z. Guo, M. You, Y. F. Deng, Q. Liu, Y. S. Meng, Z. Pikramenou and Y. Z. Zhang, An azido-bridged [FeII4] grid-like molecule showing spin crossover behaviour, *Dalton Trans.*, 2021, **50**, 14303–14308.

18 (*a*) J.-Y. Ge, Z. Chen, L. Zhang, X. Liang, J. Su, M. Kurmoo and J.-L. Zuo, A Two-Dimensional Iron(II) Coordination Polymer with Synergetic Spin-Crossover and Luminescent Properties, *Angew. Chem., Int. Ed.*, 2019, **58**, 8789–8793; (*b*) Y. R. Qiu, L. Cui, J. Y. Ge, M. Kurmoo, G. Ma and J. Su, Iron(II) Spin Crossover Coordination Polymers Derived From a Redox Active Equatorial Tetrathiafulvalene Schiff-Base Ligand, *Front. Chem.*, 2021, **9**, 9692939; (*c*) C. F. Wang, J. C. Wu and Q. Li, Synchronously tuning the spin-crossover and fluorescence properties of a two-dimensional Fe (II) coordination polymer by solvent guests, *Inorg. Chem. Front.*, 2022, **9**, 3251–3258.

19 M. Seredyuk, K. Znovjyak, F. J. Valverde-Muñoz, I. da Silva, M. C. Muñoz, Y. S. Moroz and J. A. Real, 105 K wide room temperature spin transition memory due to a supramolecular latch mechanism, *J. Am. Chem. Soc.*, 2022, **144**, 14297–14309.

20 M. Seredyuk, K. Znovjyak, F. J. Valverde-Muñoz, M. C. Muñoz, I. O. Fritsky and J. A. Real, Rotational order-disorder and spin crossover behaviour in a neutral iron(II) complex based on asymmetrically substituted large planar ionogenic ligand, *Dalton Trans.*, 2024, **53**, 8041–8049.

21 (*a*) M. M. Dîrtu, C. Neuhausen, A. D. Naik, A. Rotaru, L. Spinu and Y. Garcia, Insights into the Origin of Cooperative Effects in the Spin Transition of $[Fe(NH_2trz)_3](NO_3)_2$: the Role of Supramolecular Interactions Evidenced in the Crystal Structure of $[Cu(NH_2trz)_3](NO_3)_2{\cdot}H_2O$, *Inorg. Chem.*, 2010, **49**, 5723–5736; (*b*) C. Chong, H. Mishra, K. Boukheddaden, S. Denise, G. Bouchez, E. Collet, J. C. Ameline, A. D. Naik, Y. Garcia and F. Varret, Electronic and Structural Aspects of Spin Transitions Observed by Optical Microscopy. The Case of $Fe(ptz)_6(BF_4)_2$, *J. Phys. Chem. B*, 2010, **114**, 1975–1984.

22 S. Decurtins, P. Gütlich, C. P. Köhler, H. Spiering and A. Hauser, Light-induced excited spin state trapping in a transition metal complex: The hexakis(1-propyltetrazole) iron(II) tetrafluoroborate spin-crossover system, *Chem. Phys. Lett.*, 1984, **105**, 1–4.

23 J. F. Létard, P. Guionneau, L. Rabardel, J. A. K. Howard, A. E. Goeta, D. Chasseau and O. Kahn, Structural, magnetic, and photomagnetic studies of a mononuclear iron(II) derivative exhibiting an exceptionally abrupt spin transition. Light-induced thermal hysteresis phenomenon, *Inorg. Chem.*, 1998, **37**, 4432–4441.

24 J.-F. Létard, G. Chastanet, P. Guionneau and C. Desplanches, in *Spin-Crossover Materials*, John Wiley & Sons Ltd, 2013, pp. 475–506.

25 (*a*) M. Cavallini, I. Bergenti, S. Milita, J. C. Kengne, D. Gentili, G. Ruani, I. Salitros, V. Meded and M. Ruben, Thin deposits and patterning of room-temperature-switchable one-dimensional spin-crossover compounds, *Langmuir*, 2011, **27**, 4076–4081; (*b*) A. Abherve, M. Jose Recio-Carretero, M. Lopez-Jorda, J. Modesto Clemente-Juan, J. Canet-Ferrer, A. Cantarero, M. Clemente-Leon and E. Coronado, Nonanuclear Spin-Crossover Complex Containing Iron(II) and Iron(III) Based on a 2,6-Bis(pyrazol-1-yl)pyridine Ligand Functionalized with a Carboxylate Group, *Inorg. Chem.*, 2016, **55**, 9361–9367; (*c*) M. Attwood, H. Akutsu, L. Martin, T. J. Blundell, P. Le Maguere and S. S. Turner, Exceptionally high temperature spin crossover

in amide-functionalised 2,6-bis(pyrazol-1-yl)pyridine iron(II) complex revealed by variable temperature Raman spectroscopy and single crystal X-ray diffraction, *Dalton Trans.*, 2021, **50**, 11843–11851.

26 M. Sorai, M. Nakano and Y. Miyazaki, Calorimetric investigation of phase transitions occurring in molecule-based magnets, *Chem. Rev.*, 2006, **106**, 976–1031.

27 (*a*) M. J. Turner, S. P. Thomas, M. W. Shi, D. Jayatilaka and M. A. Spackman, Energy frameworks: insights into interaction anisotropy and the mechanical properties of molecular crystals, *Chem. Commun.*, 2015, **51**, 3735–3738; (*b*) P. R. Spackman, M. J. Turner, J. J. McKinnon, S. K. Wolff, D. J. Grimwood, D. Jayatilaka and M. A. Spackman, CrystalExplorer: a program for Hirshfeld surface analysis, visualization and quantitative analysis of molecular crystals, *J. Appl. Crystallogr.*, 2021, **54**, 1006–1011.

28 M. G. Reeves, E. Tailleur, P. A. Wood, M. Marchivie, G. Chastanet, P. Guionneau and S. Parsons, Mapping the cooperativity pathways in spin crossover complexes, *Chem. Sci.*, 2021, **12**, 1007–1015.

29 M. Seredyuk, K. Znovjyak, F. J. Valverde-Muñoz, M. C. Muñoz, V. M. Amirkhanov, I. O. Fritsky and J. A. Real, Order-disorder, symmetry breaking, and crystallographic phase transition in a series of bis(trans-thiocyanate)iron(II) spin crossover complexes based on tetradentate ligands containing 1,2,3-triazoles, *Inorg. Chem.*, 2023, **62**, 9044–9053.

30 (*a*) Z.-K. Liu, A. A. Starikova, Y.-X. Li, K. Sun, M. Yu, Z.-S. Yao and J. Tao, Illuminating spin-crossover octanuclear metal-organic cages, *Sci. China: Chem.*, 2024, **67**, 1208–1215; (*b*) C. Yi, Y.-S. Meng, L. Zhao, N.-T. Yao, Q. Liu, W. Wen, R.-X. Li, Y.-Y. Zhu, H. Oshio and T. Liu, A Smart Molecule Showing Spin Crossover Responsive Aggregation-Induced Emission, *CCS Chem.*, 2023, **5**, 915–924; (*c*) X.-R. Wu, Z.-K. Liu, M. Zeng, M.-X. Chen, J. Tao, S.-Q. Wu and H.-Z. Kou, Fluorescence emission modulation in cyanido-bridged Fe(II) spin crossover coordination polymers, *Sci. China: Chem.*, 2022, **65**, 1569–1576.

31 F. Renz, H. Spiering, H. A. Goodwin and P. Gütlich, Light-perturbed hysteresis in an iron(II) spin-crossover compound observed by the Mössbauer effect, *Hyperfine Interact.*, 2000, **126**, 155–158.

32 K. Boukheddaden, H. Fourati, Y. Singh and G. Chastanet, Evidence of Photo-Thermal Effects on the First-Order Thermo-Induced Spin Transition of [{Fe(NCSe)(py)2}2(m-bpypz)] Spin-Crossover Material, *Magnetochemistry*, 2019, **5**, 21.

33 G. Sheldrick, Crystal structure refinement with SHELXL, *Acta Crystallogr., Sect. C: Struct. Chem.*, 2015, **71**, 3–8.

